Hollow Rims from Water Drop Evaporation on Salt Substrates

Alexandra Mailleur, Christophe Pirat, Olivier Pierre-Louis, and Jean Colombani*
Institut Lumière Matière; Université de Lyon; Université Claude Bernard Lyon 1; CNRS UMR 5306; Domaine scientifique de la Doua, F-69622 Villeurbanne, France

(Received 12 July 2018; revised manuscript received 3 October 2018; published 21 November 2018)

We report on the observation of thin salt shells that form at the periphery of evaporating pure water drops on salt. Shell shapes range from rings of inclined walls to hollow toroidal rims. We interpret this phenomenon as a consequence of a molecular coffee-stain effect by which the dissolved salt is advected toward the pinned contact line where an increased evaporation takes place. The subsequent salt supersaturation in the vicinity of the triple line drives the crystallization of the shell at the liquid-air interface. This interpretation is supported by a simple model for shell growth.

DOI: 10.1103/PhysRevLett.121.214501

The coupling between wetting and growth is one of the major routes towards surface patterning, and leads to a wide variety of morphologies from the nano- to the macroscale. Interest in this pathway for nanostructure formation is largely driven by applications, e.g., in quantum computing [1,2] and miniature lasers [3]. Prominent nanoscale examples include vapor-liquid-solid (VLS) growth of semiconductor nanowires [4,5] and carbon nanotubes [6] and droplet epitaxy [7,8]. In this latter process, nanoscale rings or disks form, with a morphology appreciably resulting from wetting conditions [9].

At the macroscale, ring-shape patterns have also been obtained via the coffee-stain effect, by which the evaporation of a drop of suspension leads to a deposit at the periphery of the dried drop—similar to a coffee stain—when the triple line is pinned. This results from outward flows inside the drop compensating the enhanced loss of liquid due to a higher evaporation rate at the periphery [10–16]. Since it induces unwanted stains on dishes, or heterogeneous deposits on ultraclean surfaces in microelectronics, at first glance this phenomenon appears as detrimental. However, following the development of methods controlling the final deposit, using particle shape [17], Marangoni flow [18], liquid viscosity [19], or drop size [20], this effect is now considered to be a promising surface patterning technique [21,22].

Models both at the nano- and macroscales have confirmed that a large variety of final deposit shapes can be reached. For example, ringlike to mountainlike morphologies can be obtained by varying the triple line mobility [23], and multiple rings can be found in droplet epitaxy [8,9,24]. Molecular simulations of microdroplet evaporation on soluble substrates also suggest the formation of rims [25].

We propose in this Letter a configuration where the interplay between drop wetting and material dissolution and growth leads to an unexpected surface morphology. We show that when a sessile millimeter-size drop of water evaporates on a soluble substrate, dissolution and evaporation can proceed simultaneously, and the dissolved species precipitate as a ring-shaped stain. This peripheral deposit exhibits a unique morphology with an open or closed hollow shell, in striking contrast with deposits from salty water evaporating on inert substrates [26,27] or pure water evaporating on hydrosoluble solids [28,29]. Furthermore, our experiments demonstrate that the coffee-stain effect may even occur with a pure solvent, such as water, instead of a prepared liquid, provided that the solid dissolves in the liquid.

We present here observations of deposits obtained in various experimental conditions. The data are interpreted in the frame of a simple analytical model, taking into account four basic ingredients: (i) evaporation at the liquid-air interface, (ii) dissolution at the solid-liquid interface, (iii) diffusion and convection inside the liquid, and (iv) precipitation at the edge of the drop. We propose thereby a nonequilibrium morphology diagram that depends on the contact angle and on the ratio between drop radius and shell thickness. Finally, we speculate that the thickness of the shell should be controlled by a competition between mass transport kinetics and solid-liquid surface tension.

In all experiments, the substrate is a $10 \times 10 \times 1$ mm^3 NaCl single crystal, polished with grit size down to 1 μm in dry conditions. Salt residues are removed by a burst of compressed air. This polishing protocol leads to a roughness of $\sim$100 nm measured by atomic force microscopy (AFM). The evaporation proceeds in a closed $240 \times 240 \times 300$ mm^3 vessel in which the substrate lies on a copper disk, the temperature of which is regulated by a heating resistance and a thermal platinum probe, in the range from 20 to 80 °C. The disk presents 32 notches, containing one sample each. After each drop evaporation, the disk is properly rotated and the next drop is deposited.

Moisture in the cell is controlled by a wide beaker of saturated solution of various inorganic salts and monitored

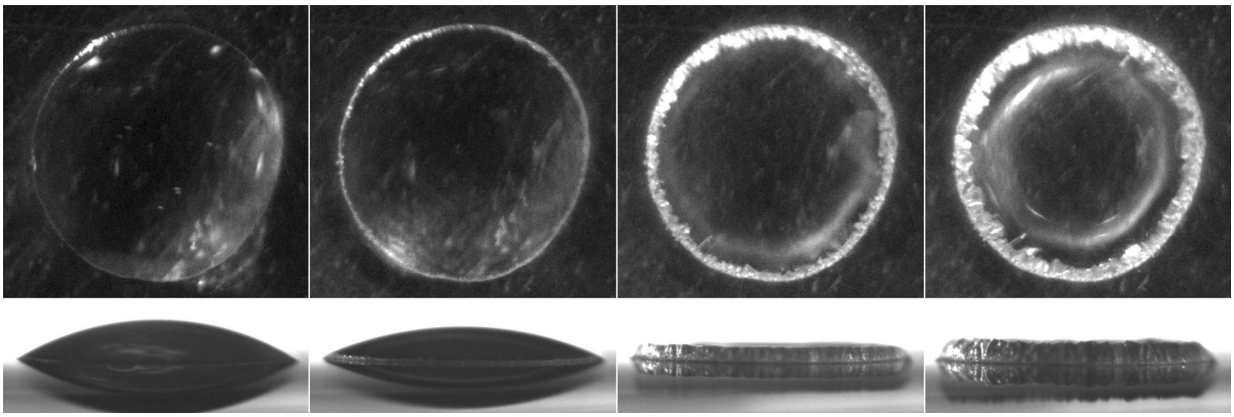

FIG. 1. Top and side views of a drop of water evaporating at 55 °C on a polished NaCl single crystal seen 2, 13, 23, and 33 s after deposition (from left to right). The sessile diameter of the drop is 2.0 mm.

with a hygrometer (see schematic of the setup in Fig. S1 in Supplemental Material [30]). The relative humidity ranges from 18% to 45%. The drop, of initial volume ranging from 0.05 to 3.5 μl, corresponding to an initial sessile diameter between 1.0 and 3.7 mm, is deposited with a needle and its evaporation is recorded from the side and from the top. The deposited liquid is always ultrapure water. Evaporation times, depending on temperature, relative humidity, drop size, and contact angle, span from 10 to 300 s. The dryouts are observed *post mortem* with scanning electron microscopy (SEM) and their topography is measured with a vertical scanning interferometry (VSI) profilometer.

Figure 1 displays snapshots of the evaporating drop at 55 °C (see videos in Supplemental Material [30]). Simultaneous water evaporation and salt precipitation in a peripheral rim are observed. The transfer of salt from the drop to the outer deposit shows, as for colloidal suspensions, that the divergence of the evaporation flux at the anchored triple line induces an outward capillary flow [31]. Depending on experimental conditions, as shown in Figs. 2 and 3, these rims exhibit a variety of shapes that range from open deposits in the form of a continuous inclined wall to closed deposits, with a truncated toroidal shape. Additionally, the relief of the dryout has been investigated with VSI (see an example in Fig. S2 in the Supplemental Material [30]).

Among the varied parameters, the drop radius and contact angle have appeared to be the driving ones (see model below). Nevertheless, it should be noted that we have seen no impact of the temperature on the morphology, except the absence of closed shells for a vanishing temperature gradient between drop and substrate.

The evaporation scenario leading to the formation of these shells can be divided into four stages. (i) In all experiments, at the drop deposition, the triple line is pinned, an immediate dissolution of the substrate occurs, and a deposit starts to precipitate at the anchored three-phase line (first image in Fig. 1). We observe in the profilometric image (Fig. S2 in Supplemental Material [30]) that the substrate is dug in the middle of the stain after evaporation. The height of the drop is of the order $h \sim 100$ μm and the diffusion coefficient of the salt in the drop is $D \sim 10^{-9}$ m^2/s at ambient temperature. Therefore the formation of this central depression caused by dissolution, and the resulting saturation in salt of water, must appear after a time $\tau = h^2/D \sim 10$ s. At ambient temperature, the evaporation time is always larger than 1 min, so the saturation of the liquid by diffusion occurs at the very beginning of the experiment. As both the diffusion coefficient and evaporation rate increase with temperature, this should remain true at all temperatures. (ii) During evaporation, the three-phase line leaves the initial perimeter of the drop and remains attached to the edge of the growing deposit (second image in Fig. 1) [32]. (iii) Approaching the end of the experiment, the drop surface becomes concave, and the

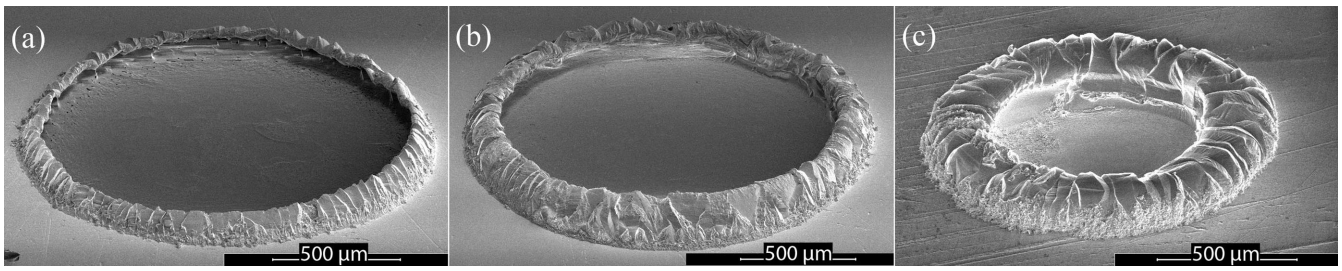

FIG. 2. SEM images of deposits with different morphologies: (a) open shell, (b) intermediate open shell, and (c) closed shell.

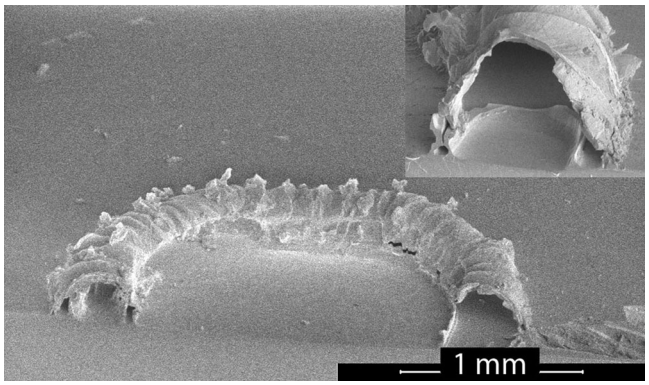

FIG. 3. Sliced deposit showing (inset) a hollow crystalline rim, the membrane of which is roughly 15 μm thick.

drop surface in the center reaches the salt substrate. A new inner triple line then recedes outwards, until it reaches the deposit (see video from the top in the Supplemental Material [30] for a clearer view of the phenomenon). During this stage, the deposit may close to form a hollow shell, or remain under the form of inclined walls. In all cases, a striking pattern of linear defects oriented roughly along the radial direction is also observed on the shell (see Fig. S3 in the Supplemental Material for images of this effect [30]). (iv) At the very end of the evaporation process, the remaining liquid recedes inside the hollow shell (see video from the top in the Supplemental Material [30]).

In order to analyze this original shell formation mechanism, we have designed a minimal model, inspired by the approach of Deegan *et al.* [31]. We assume that the evaporation flux is larger at the edge of the drop, and this inhomogeneity of evaporation drives an outward radial hydrodynamic flow. This leads to a supersaturation in the triple-line region, which feeds the growth of the shell. Considering an axisymmetric drop shape, global mass conservation and salt mass conservation impose two integral relations, respectively:

$$0 = \int_{r_0}^{r_{\mathrm{TL}}} dr 2\pi r[\partial_t h(r) + J_s(r)], \tag{1}$$

$$-2\pi r_{\mathrm{TL}} w \partial_t r_{\mathrm{TL}} = \int_{r_{\mathrm{TL}}-ah_{\mathrm{TL}}}^{r_{\mathrm{TL}}} dr 2\pi r \Omega c_{\mathrm{eq}}[\partial_t h(r) + J_s(r)], \tag{2}$$

where, as illustrated in the schematic in Fig. 4, $h(r)$ is the liquid-gas surface profile, $J_s(r)$ is the evaporation rate, r_{TL} is the radius of the liquid-gas interface, and h_{TL} is the height of the edge of the shell. These relations also include the shell thickness w, the molecular volume Ω of the salt, and its solubility c_{eq} in water. We have neglected the possible change in the depth of the substrate under the drop, which is assumed to be small compared to the change of height of the liquid-gas interface [30]. The second relation assumes

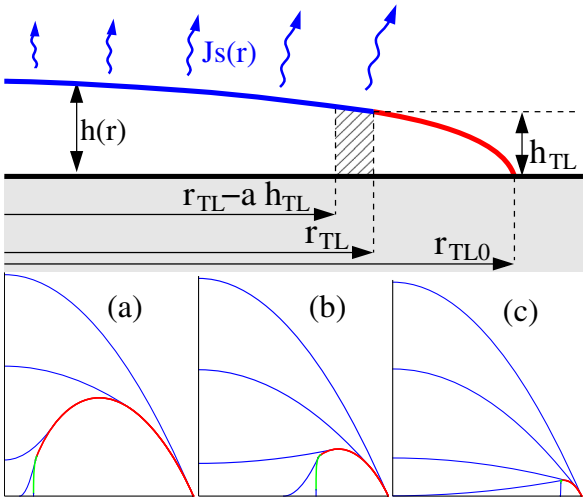

FIG. 4. Top: schematic of the model. Bottom: shell formation dynamics. (a) $r_{\mathrm{TL0}} = 0.5$ mm (closed), (b) $r_{\mathrm{TL0}} = 1$ mm (closed), (c) $r_{\mathrm{TL0}} = 2$ mm (open). Images obtained with model II in the third stage of the dynamics, and assuming $a = 1$, $\Omega c_{\mathrm{eq}} = 0.26$, $w = 20$ μm, and initial contact angle $\sin\theta = 0.4$. The thick red line represents the shell formed in the second stage, and the thick green line represents the shell formed in the third stage. The thin blue lines represent the liquid-gas interface at 0%, 40%, 80%, 97%, and 100% of the total time.

that all the salt arriving in the zone $r_{\mathrm{TL}} - ah_{\mathrm{TL}} < r < r_{\mathrm{TL}}$, indicated by the shaded area in the schematic of Fig. 4, is incorporated into the shell. The phenomenological dimensionless constant a accounts for the diffusion-induced three-dimensional redistribution of mass around the edge of the shell.

As observed in experiments, the evaporation process can be decomposed into four stages. In the second stage, the liquid-air interface profile can be approximated by a parabola: $h(r) = h_{\mathrm{TL}} + (r_{\mathrm{TL}}^2 - r^2)/2R$ with R the radius of curvature of the drop and $r_0 = 0$ in Eq. (1). Assuming tangential growth of the shell along the drop surface (as in the second image of Fig. 1), and an evaporation flux $J_s(r) \approx J_0/(1 - r^2/r_{\mathrm{TL}}^2)^{1/2}$, with J_0 the evaporation flux away from the triple line, within the small slope approximation [31], we obtain two coupled equations from Eqs. (1), (2) in the limit $ah_{\mathrm{TL}} \ll r_{\mathrm{TL}}$

$$\frac{\partial_t R}{J_0} = 8\frac{R^2}{r_{\mathrm{TL}}^2}, \tag{3}$$

$$\frac{\partial_t r_{\mathrm{TL}}}{J_0} = \Omega c_{\mathrm{eq}} \frac{(2a r_{\mathrm{TL}})^{1/2}}{w}\left(\frac{r_{\mathrm{TL0}}^2}{2R_0} - \frac{r_{\mathrm{TL}}^2}{2R} - 4J_0 t\right)^{1/2}, \tag{4}$$

where $r_{\mathrm{TL0}} = r_{\mathrm{TL}}(t = 0)$ and $R_0 = R(t = 0)$. These equations are solved numerically.

In the third stage, where the drop is ring shaped, the radius of the uncovered zone in the center of the drop is denoted as r_{in}. Once again, the profile is assumed to be a

constant mean-curvature surface. Assuming in addition a vanishing contact angle at $r = r_{\rm in}$, we obtain $h(r) = h_{\rm TL} f(r)/f(r_{\rm TL})$, where $f(r) = (r^2 - r_{\rm in}^2)/2 - r_{\rm in}^2 \ln(r/r_{\rm in})$, and $r_0 = r_{\rm in}$ in Eq. (1). We consider two models for evaporation (see Supplemental Material for details [30]). The first model (model I) accounts for an increase of evaporation at the inner triple line of radius $r = r_{\rm in}$. In contrast, the second one (model II) still uses the same expression of the evaporation rate as in the first stage. While both models lead to considerable complication of the dynamical equations as compared to the second stage, they do not bring significant changes from the results of the second stage. Indeed, due to the smallness of the liquid volume in the third stage, the additional growth of the shell is relatively small.

As in the experiments, the resulting shell shapes are found to be closed or open depending on model parameters, as shown in Fig. 4. The simulations are stopped when the distance between the two triple lines $r_{\rm TL} - r_{\rm in}$ is equal to the cutoff length $a h_{\rm TL}$. We consider that shells are closed when the final value of $h_{\rm TL}$ is less than 20% of the maximum shell height. Movies of the modeled dynamics are presented in the Supplemental Material [30]. As seen by a rescaling of time in Eqs. (3) and (4), the evaporation rate J_0 determines the timescale of the evolution, but does not affect the morphology of the shell. The shapes depend only on two dimensionless parameters, $\sin\theta_0 = r_{\rm TL0}/R_0$ and $\alpha = a^{1/2}\Omega c_{\rm eq} r_{\rm TL0}/w$. A nonequilibrium morphology phase diagram is reported in Fig. S5 of the Supplemental Material [30] for the two models.

Experimentally, Ω and $c_{\rm eq}$ are constant, and the initial contact angle θ_0 and the initial sessile drop radius $r_{\rm TL0}$ are the control parameters. The variability of the shell thickness w has to be assessed to test the model. To estimate this quantity, it has been considered that, when the deposit is closed, it forms a truncated torus of external radius $r_{\rm TL0}$, width Φ, and thickness w. The volume of deposited salt in the shell is $V_t \simeq \pi\Phi w(2r_{\rm TL0} - \Phi)\theta/\sin(\theta)$ for $w \ll \Phi$, $r_{\rm TL0}$. This volume corresponds to the total dissolved volume $V_{\rm diss}$. Using our VSI experiments, we have measured the volume of the central depression, i.e., the volume of dissolved salt $V_{\rm diss}$, and the deposit width Φ, for all drops. Considering $\theta \simeq \pi/4$ (see Fig. 5), we have thereby plotted $V_{\rm diss}$ against $\pi^2\Phi(2r_{\rm TL0} - \Phi)/(2\sqrt{2})$ (see Fig. S4 in Supplemental Material [30]). The dots are aligned along a straight line, proving that the shell thickness has a roughly constant value, the best fit of which is $w \simeq 17$ μm. SEM images of the shell confirm this value (see Fig. 3).

In Fig. S4, no strong correlation can be observed between the temperature and the position of the dots, showing an absence of an apparent link between the temperature and the shell thickness. This result is in line with our model, in which the temperature only drives the characteristic time of the experiment (mainly via J_0), without influencing the morphology selection.

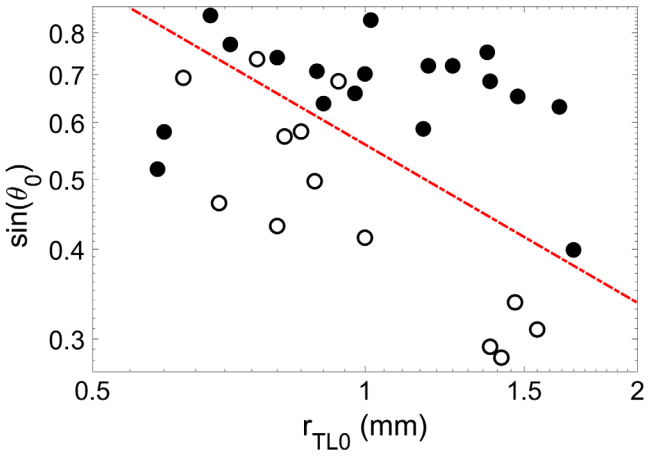

FIG. 5. Sine of the initial contact angle θ_0 vs initial sessile drop radius $r_{\rm TL0}$. Open dots stand for wall-like deposits and full dots for truncated toroidal deposits. The dashed line is the prediction of the model for the boundary between both morphologies (with model II in the third stage of the dynamics), assuming $a = 1.4$, $\Omega c_{\rm eq} = 0.26$ and $w = 17$ μm.

Experimentally, the only varying parameter in α is $r_{\rm TL0}$, so the model predicts that the open and closed morphologies correspond to distinct regions in the $\sin\theta_0$–$r_{\rm TL0}$ plane. This prediction is clearly verified in Fig. 5.

We now propose a first explanation of the order of magnitude of the shell thickness. A back-of-the-envelope analysis shows that this thickness cannot be fixed by the competition between the salt precipitation rate, and the diffusion of the dissolved material (see Supplemental Material [30] for details). Inspired by standard analysis of growth instabilities leading to the formation of dendrites and other patterns, another possible candidate for the selection of the shell thickness is the competition between diffusion-limited mass transport and the solid-liquid surface tension γ. Elaborating on this analogy, the growth of the edge of the shell would be driven by the evaporation induced convective transport of salt with the flux $\sim J_s(r = r_{\rm TL} - w)\Omega c_{\rm eq}/(1 - \Omega c_{\rm eq})$, where $J_s(r = r_{\rm TL} - w) \approx (r_{\rm TL}/2w)^{1/2} J_0$ when $w \ll r_{\rm TL}$. However, the curvature $\kappa \sim 1/w$ of the edge of the shell leads to an increase of the chemical potential by $\Delta\mu = \Omega\gamma\kappa$. Since concentration gradients occur at a scale $\sim w$, this chemical potential rise drives a diffusion-limited dissolution rate $\sim(D\Omega c_{\rm eq}/w)(\Delta\mu/k_B T)$, where k_B is the Boltzmann constant and T the temperature. Combining this dissolution rate with the convection-induced mass supply, we obtain an estimate of the edge velocity $v \sim J_0 (r_{\rm TL}/2w)^{1/2}\Omega c_{\rm eq}/(1 - \Omega c_{\rm eq}) - D\Omega^2 c_{\rm eq}\gamma/(w^2 k_B T)$. Assuming a selection of w based on the maximization of v, we find

$$w = \frac{2^{5/3}}{r_{\rm TL}^{1/3}} \left(\frac{(1 - \Omega c_{\rm eq})\Omega D\gamma}{k_B T J_0} \right)^{2/3}. \tag{5}$$

Taking $\gamma \sim 0.1\ \mathrm{J\,m^{-2}}$, and $\Omega \sim 10^{-28}\ \mathrm{m^3}$, we find $w \sim 3\ \mu\mathrm{m}$, which is of the same order of magnitude as the experimental value $\sim 17\ \mu\mathrm{m}$. The related growth velocity $v_{\max} \sim J_0(r_{\mathrm{TL}}/2w)^{1/2}\Omega c_{\mathrm{eq}}/(1-\Omega c_{\mathrm{eq}}) \sim \mu\mathrm{m\,s^{-1}}$, is also in reasonable agreement with experimental observations. In the Supplemental Material [30], we show that attachment-detachment-limited kinetics lead to similar orders of magnitude as diffusion limited kinetics.

In conclusion, we have shown that the coffee-stain effect, observed in an extensive number of complex fluids, can also be obtained with initially pure water, provided that it evaporates on a rapidly dissolving solid, a salt, for example. The dryout is always composed of a thin shell, either open, or closed in the form of a hollow rim, depending on the drop radius and contact angle. This experimental configuration proves in a novel and unexpected way the potentialities of the wetting-growth coupling in materials science.

We thank David Brutin for enlightening discussions, Gilles Simon, François Gay, Charlotte Rivière, Rémy Fulcrand, and Agnès Piednoir for experimental help, and CNES (French Space Agency) and CNRS for financial support.

*jean.colombani@univ-lyon1.fr

[1] D. Loss and D. P. DiVincenzo, Quantum computation with quantum dots, Phys. Rev. A **57**, 120 (1998).
[2] S. Nadj-Perge, S. M. Frolov, E. P. A. M. Bakkers, and L. P. Kouwenhoven, Spin-orbit qubit in a semiconductor nanowire, Nature (London) **468**, 1084 (2010).
[3] M. S. Gudiksen, L. J. Lauhon, J. Wang, D. C. Smith, and C. M. Lieber, Growth of nanowire superlattice structures for nanoscale photonics and electronics, Nature (London) **415**, 617 (2002).
[4] P. Yang, H. Yan, S. Mao, R. Russo, J. Johnson, R. Saykally, N. Morris, J. Pham, R. He, and H. J. Choi, Controlled growth of ZnO nanowires and their optical properties, Adv. Funct. Mater. **12**, 323 (2002).
[5] S. Kodambaka, J. Tersoff, M. C. Reuter, and F. M. Ross, Germanium nanowire growth below the eutectic temperature, Science **316**, 729 (2007).
[6] K. W. Schwarz and J. Tersoff, From Droplets to Nanowires: Dynamics of Vapor-Liquid-Solid Growth, Phys. Rev. Lett. **102**, 206101 (2009).
[7] K. Watanabe, N. Koguchi, and Y. Gotoh, Fabrication of GaAs quantum dots by modified droplet epitaxy, Jpn. J. Appl. Phys. **39**, L79 (2000).
[8] T. Mano, T. Kuroda, S. Sanguinetti, T. Ochiai, T. Tateno, J. Kim, T. Noda, M. Kawabe, K. Sakoda, G. Kido *et al.*, Self-assembly of concentric quantum double rings, Nano Lett. **5**, 425 (2005).
[9] Z. Y. Zhou, C. X. Zheng, W. X. Tang, J. Tersoff, and D. E. Jesson, Origin of Quantum Ring Formation during Droplet Epitaxy, Phys. Rev. Lett. **111**, 036102 (2013).
[10] R. Deegan, O. Bakajin, T. Dupont, G. Huber, S. Nagel, and T. Witten, Capillary flow as the cause of ring stains from dried liquid drops, Nature (London) **389**, 827 (1997).
[11] C. Annarelli, J. Fornazero, J. Bert, and J. Colombani, Crack patterns in drying protein solution drops, Eur. Phys. J. E **5**, 599 (2001).
[12] T. Yakhno, Salt-induced protein phase transitions in drying drops, J. Colloid Interface Sci. **318**, 225 (2008).
[13] Y. Tarasevich, I. Vodolazskaya, and O. Bondarenko, Modeling of spatial–temporal distribution of the components in the drying sessile droplet of biological fluid, Colloids Surf. A **432**, 99 (2013).
[14] B. Sobac and D. Brutin, Desiccation of a sessile drop of blood: Cracks, folds formation and delamination, Colloids Surf. A **448**, 34 (2014).
[15] C. Sadek, L. Pauchard, P. Schuck, Y. Fallourd, N. Pradeau, C. L. Floch-Fouéré, and R. Jeantet, Mechanical properties of milk protein skin layers after drying: Understanding the mechanisms of particle formation from whey protein isolate and native phosphocaseinate, Food Hydrocolloids **48**, 8 (2015).
[16] P. Sáenz, A. Wray, Z. Che, O. Matar, P. Valluri, J. Kim, and K. Sefiane, Dynamics and universal scaling law in geometrically-controlled sessile drop evaporation, Nat. Commun. **8**, 14783 (2017).
[17] P. J. Yunker, T. Still, M. A. Lohr, and A. G. Yodh, Suppression of the coffee-ring effect by shape-dependent capillary interactions, Nature (London) **476**, 308 (2011).
[18] H. Hu and R. Larson, Marangoni effect reverses coffee-ring depositions, J. Phys. Chem. B **110**, 7090 (2006).
[19] C. Chon, S. Paik, J. Tipton, and K. Kihm, Effect of nanoparticle sizes and number densities on the evaporation and dryout characteristics for strongly pinned nanofluid droplets, Langmuir **23**, 2953 (2007).
[20] X. Shen, C.-M. Ho, and T.-S. Wong, Minimal size of coffee ring structure, J. Phys. Chem. B **114**, 5269 (2010).
[21] K. Sefiane, Patterns from drying drops, Adv. Colloid Interface Sci. **206**, 372 (2014).
[22] Droplet Wetting and Evaporation, edited by D. Brutin (Elsevier, Amsterdam, 2015).
[23] X. Man and M. Doi, Ring to Mountain Transition in Deposition Pattern of Drying Droplets, Phys. Rev. Lett. **116**, 066101 (2016).
[24] X. L. Li, Formation mechanisms of multiple concentric nanoring structures upon droplet epitaxy, J. Phys. Chem. C **114**, 15343 (2010).
[25] R. Cordeiro and T. Pakula, Behavior of evaporating droplets at nonsoluble and soluble surfaces: Modeling with molecular resolution, J. Phys. Chem. B **109**, 4152 (2005).
[26] N. Shahidzadeh-Bonn, S. Rafaï, D. Bonn, and G. Wegdam, Salt crystallization during evaporation: Impact of interfacial properties, Langmuir **24**, 8599 (2008).
[27] N. Shahidzadeh, M. Schut, J. Desarnaud, M. Prat, and D. Bonn, Salt stains from evaporating droplets, Sci. Rep. **5**, 10335 (2015).
[28] A. Tay, D. Bendejacq, C. Monteux, and F. Lequeux, How does water wet a hydrosoluble substrate?, Soft Matter **7**, 6953 (2011).
[29] J. Dupas, E. Verneuil, M. Ramaioli, L. Forny, L. Talini, and F. Lequeux, Dynamic wetting on a thin film of soluble

polymer: Effects of nonlinearities in the sorption isotherm, Langmuir **29**, 12572 (2013).

[30] See Supplemental Material at http://link.aps.org/supplemental/10.1103/PhysRevLett.121.214501 where a schematic of the experiment, experimental and numerical videos of the evaporating drop, a dryout profile, a complement about the defect pattern on the shell, complements about the model, a shell tickness estimation, and a numerical morphology diagram are provided.

[31] R. D. Deegan, O. Bakajin, T. F. Dupont, G. Huber, S. R. Nagel, and T. A. Witten, Contact line deposits in an evaporating drop, Phys. Rev. E **62**, 756 (2000).

[32] G. Berteloot, A. Hoang, A. Daerr, H. Kavehpour, F. Lequeux, and L. Limat, Evaporation of a sessile droplet: Inside the coffee stain, J. Colloid Interface Sci. **370**, 155 (2012).